Article

Experimental Investigation of the Mechanical and Electrical Failure of the Electrode Tab of Lithium-Ion Pouch Cells Under Quasi-Static Mechanical Load

Patrick Höschele * , Simon Franz Heindl and Christian Ellersdorfer

Vehicle Safety Institute, Graz University of Technology, 8010 Graz, Austria; simon.heindl@tugraz.at (S.F.H.);
christian.ellersdorfer@tugraz.at (C.E.)
* Correspondence: patrick.hoeschele@tugraz.at

Abstract: The electrode tabs of pouch cells are rigidly joined to the bus bar in a battery module to achieve an electric connection. The effect of abusive mechanical loads arising from crash-related deformation or the possible movement of battery cells caused by operation-dependent thickness variations has so far never been investigated. Three quasi-static abuse tests for the anode and cathode electrode tabs were conducted with pouch cells at 100% SOC. Tensile tests on the anode, cathode and pouch foil were performed in order to explain differences between the anode and cathode in the abuse tests. The experiments revealed different failure mechanisms for the anode and cathode electrode tabs. The cathode failed at an average maximum load of 940.3 N through an external rupture of the electrode tab. The anode failed at an average maximum load of 868.9 N through a rupture of the single electrode sheets and the opening of the pouch foil. No thermal runaway occurred for either cathode or anode. The results of this study reveal a more critical failure behavior for the anode electrode tab, which can be addressed in the future by adding a predetermined breaking point and adapting the geometry of the anode electrode tab.

Keywords: lithium-ion battery; pouch cell; current conductor flag; electrode tab; quasi-static; mechanical abuse load; tensile tests; electro-mechanical failure

1. Introduction

Lithium-ion batteries (LIBs) have been widely used as energy storage systems, especially in electric vehicles (EVs) [1]. In addition to advantages such as high energy density and long cycle life, LIB technology also poses safety-related risks such as thermal runaway [2]. Pouch cells have great potential due to higher useful mass when compared to other battery cell formats like prismatic or cylindrical cells [3]. Intrinsic to pouch cells is the low mechanical stiffness. Therefore, an appropriate mechanical integration into the battery system (e.g., the module) must be achieved in order to guarantee safe operation under normal operation conditions and also in the case of abusive mechanical loads (e.g., crashes) [4–6].

Pouch cells have a negative and positive electrode tab arranged either on the same edge or on opposite edges to make an electric connection [7,8]. The electrode tabs have to fulfil several requirements such as low resistance [9], high current-carrying capacity and specific thermal capacity or design to achieve a temperature homogeneity of the battery cell [10,11]. The anode or cathode electrode tab normally consists of a nickel-coated copper or aluminum plate [12,13].

The single electrode sheets of the anode or cathode consist of the area with active material and a current conductor flag without an active material coating. The current conductor flags of the single electrode sheets are mostly welded together via ultrasonic welding or laser beam welding onto the corresponding electrode tab (anode or cathode) [14–16]. The

welding parameters highly affect the electrical performance of the welded area and also the mechanical properties [14,16].

A bus bar connects the anode or cathode electrode tabs of the single cells in a battery module according to the desired cell interconnection (e.g., parallel or serial). Ultrasonic welding, laser beam welding, resistance welding, friction stir welding or soldering are mostly used to establish a performant electrical connection between the electrode tabs and the bus bar [17–22].

The rigid and stiff connection between the bus bar and the tabs of the single cells is favorable from an electrical point of view but leads to mechanical loads when a relative motion occurs; see Figure 1. A relative motion between the bus bar and tabs can result from crash loads (e.g., deformation, acceleration) [23,24] and potentially cause an external short circuit by direct contact with electrode tabs, or an internal short circuit by an electric contact between positive and negative electrode sheets. Additionally, for pouch cells, a large relative motion within the battery module could cause a rupture of the pouch cell and pouch foil, leading to electrolyte leakage. Apart from relative motions caused by crash loads, reversible and irreversible thickness variations arising from Lithium intercalation or aging mechanisms (e.g., solid electrolyte interface growth, Lithium plating) [25,26] might result in a relative motion of battery cells in the battery module.
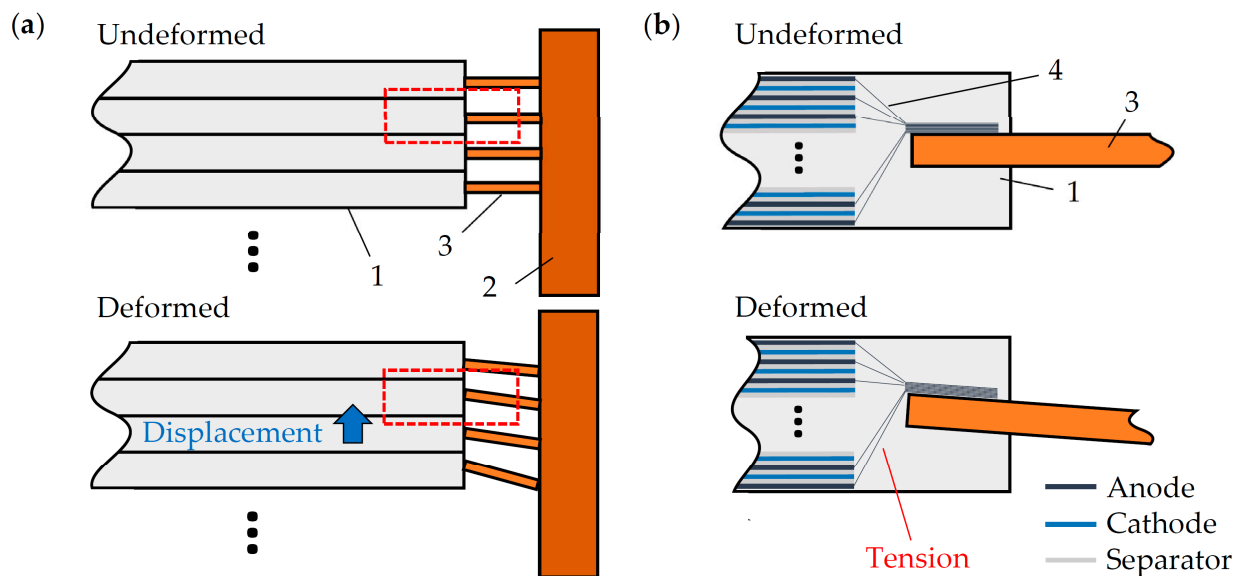
Figure 1. Principle sketch of kinematic of pouch cell (1), stack with busbar (2), electrode tabs (3) and detailed view with current conductor flags (4). (**a**) Stack level. (**b**) Detailed section indicated by red boxes.

The weld at the current conductor flags is prone to damage from vibrations, deformations and thermal fatigue [17,22]. Damage to the weld results in an increased electric resistance, causing a local heat generation [18]. The mechanical loads on the tab area might potentially lead to an internal or external short circuit, causing severe consequences like a thermal runaway [27,28].

Several norms address the safety of battery cells, but no test specifications can be found for the area of the electrode tabs [29,30]. Specific investigations into the mechanical failure behavior of battery cells under abusive loads have been reported in the literature. Zhu et al. [31], for instance, reviewed publications about mechanical tests and safety-focused simulation models. Mechanical testing was performed with welded electrode foil stacks [14,16,32] or electrode-tab-to-bus-bar connections [12,18]. However, the area of the electrode tab and current conductor flags of a pouch cell has, to the knowledge of these authors, never been mechanically characterized nor evaluated on a battery cell level with respect to safety-relevant behavior. In particular, the failure mechanisms of the electrode

tab area under large deformations (e.g., crash deformation) are relevant for investigation to avoid safety issues like electrolyte leakage or external and internal short circuits.

In this study, the electrode tab area of a commercial pouch cell was investigated for the first time. Mechanical loads on the electrode tabs might cause a severe failure when exceeding the load limits of the current conductor flags used for the electric connection of the single electrodes. The load limits of the electrode tabs for a mechanical load are unknown, although a mechanical loading cannot be avoided during the lifetime of a battery module (e.g., relative movement by thickness variation of a battery cell or crash deformation). The objective of this study is the investigation of the load limits of the electrode tab area of a pouch cell, the corresponding failure mechanisms and a safety-relevant evaluation in order to assess whether a consideration of this load case is necessary in the future.

2. Materials and Methods

Quasi-static tests were performed with six fresh pouch cells via the mechanical loading of the clamped electrode tab. Three tests were conducted on the negative electrode tab (anode) or on the positive electrode tab (cathode), in order to evaluate differences in the mechanical behavior and the failure mode. The pouch cells were charged to 100% SOC before the mechanical tests in order to evaluate the safety-relevant behavior and investigate whether a thermal runaway occurs. Tensile tests were performed on the anode electrode, cathode electrode and pouch foil in order to explain potential differences in the mechanical behavior of the quasi-static tests on the electrode tabs.

2.1. Specimen

Commercial Lithium-ion pouch cells with a capacity of 36 Ah and a weight of 860 g were used in this study. The used pouch cells were fresh and were not subjected to any cycling before the quasi-static mechanical tests were performed. The active material of the anode and cathode consisted of graphite and Nickel Manganese Cobalt Oxide (NMC), with a stoichiometric composition of NMC111 ($LiNi_{0.33}Mn_{0.33}Co_{0.33}O_2$). The pouch cell had a dimension of $325 \times 135 \times 11.2$ mm. Additional information about the tested specimen can be taken from Table 1.

Table 1. Data for tested specimen.

Parameter	Value
Nominal capacity	36 Ah
Dimension	$325 \times 135 \times 11.2$ mm
Dimension electrode stack	270×105 mm
Cathode/anode material	NMC111/graphite
Max. voltage	4.15 V
Min. voltage	2.50 V
Anode thickness *	120 μm
Copper foil thickness	10 μm
Cathode thickness *	160 μm
Aluminum foil thickness	20 μm
Separator thickness	20 μm
Layers of cathodes/anodes	31/32
Pouch foil thickness	150 μm

* Total thickness with active material and electrode carrier foil.

The anode had copper as the electrode carrier foil, with a thickness of 10 μm. The electrode tab of the anode was a nickel-coated copper plate (C1020-99.9%, HO, electroplated Ni 2.5) with a thickness of 0.3 mm. The cathode had aluminum as the electrode carrier foil, with a thickness of 20 μm. The electrode tab of the cathode was a coated aluminum plate (A1050-99.5%, HO, polymer-material-coated) with a thickness of 0.4 mm. A dissection of the pouch cell revealed that the single electrode carrier foils were welded to the electrode

tabs via ultrasonic welding; see Figure 2. The single electrode carrier foils were welded from one side to the corresponding electrode tab, resulting in an asymmetric structure.
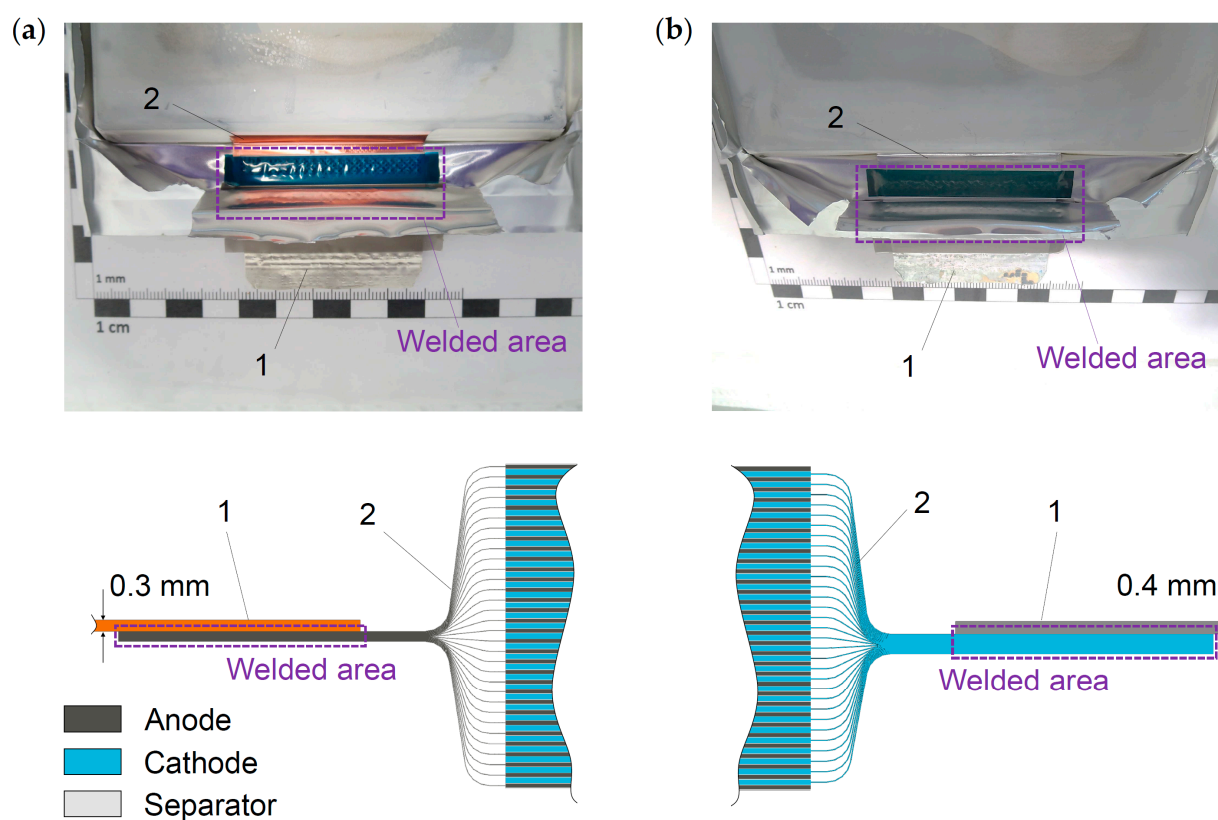

Figure 2. Dissection and principle sketch (non-proportional) of the tested specimen with detailed view of the electrode tab area with electrode tab (1) and electrode carrier foil (2). (**a**) Negative electrode tab (anode). (**b**) Positive electrode tab (cathode).

2.2. Component Tensile Tests

Tensile tests were performed on the anode and cathode electrode sheets and on the pouch foil. The geometry of the tensile test specimen can be taken from Figure 3a. One pouch cell was opened in an ambient atmosphere, and thirty tensile test specimens were prepared using the anode and cathode electrodes with a special tensile specimen punch. Twenty tensile specimens were taken from the machine direction (MD) and ten tensile specimens from the transverse direction (TD); see Figure 3b. The tensile test specimens were tested with active material as it was not possible to remove the active material without damaging the carrier foil. Ten tensile specimens were prepared from the pouch foil; see Figure 3c.

The tensile tests were performed with a universal testing machine (Zwick Roell Z010, ZwickRoell GmbH & Co. KG, Ulm, Germany) with a speed of 0.1 mm/s, to achieve quasi-static conditions. The maximum force at the point of failure and the displacement at the point of failure were statistically evaluated. The interquartile ranges and minimum and maximum values of the tests were calculated per condition (e.g., MD and TD).
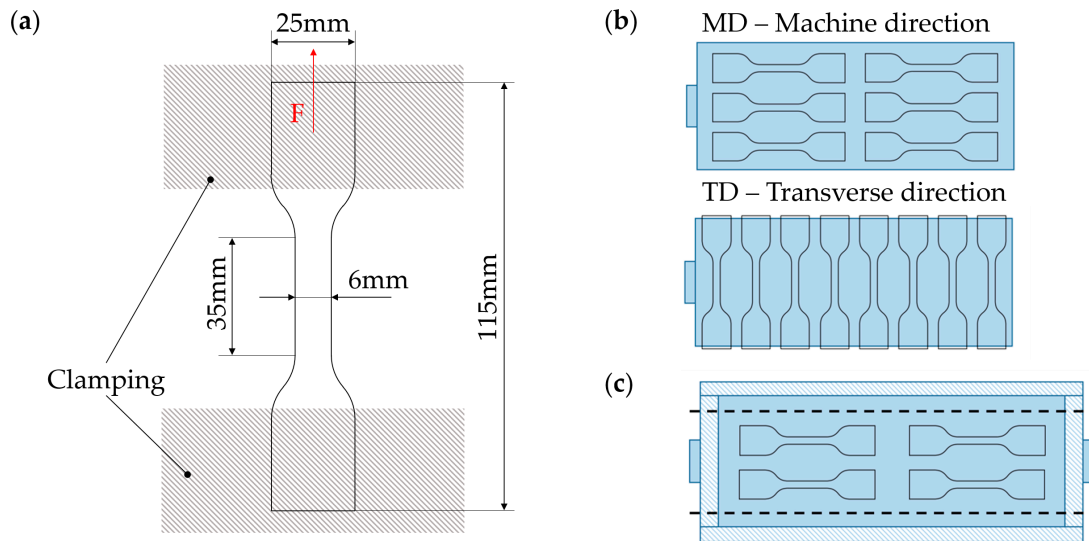
Figure 3. (**a**) Geometry of tensile specimen. (**b**) Machine direction (MD) and transverse direction (TD) for anode and cathode specimens. (**c**) Specimen from pouch foil with cutting lines indicated by dotted lines.

2.3. Quasi-Static Mechanical Tests

A test setup was designed in order to apply a shear load to the electrode tabs of the pouch cells with a hydraulic press. Figure 4 illustrates the test setup used for the quasi-static mechanical tests. The test setup consisted of a bottom plate (1) and a top plate (2). The bottom plate was bolted to a vertical connector (3) that was connected to the bottom plate of the hydraulic press. The pouch cell was placed between the bottom plate (1) and top plate (2), and a preload force of 1 kN (35.3 kPa) was applied to the electrode stack surface of 270×105 mm (see Table 1) by bolting both plates together with 10 equally distributed bolts (M8). The orientation of the pouch cell was chosen in a way that the electrode tab faced the positive z-direction with the electrode foils welded below the electrode tab; see Figure 2. A reproducible placement of the pouch cell was guaranteed through the use of guiding plates. The electrode tab was clamped with the vertical tab-clamping plate (4) that was connected to the top plate of the hydraulic press.
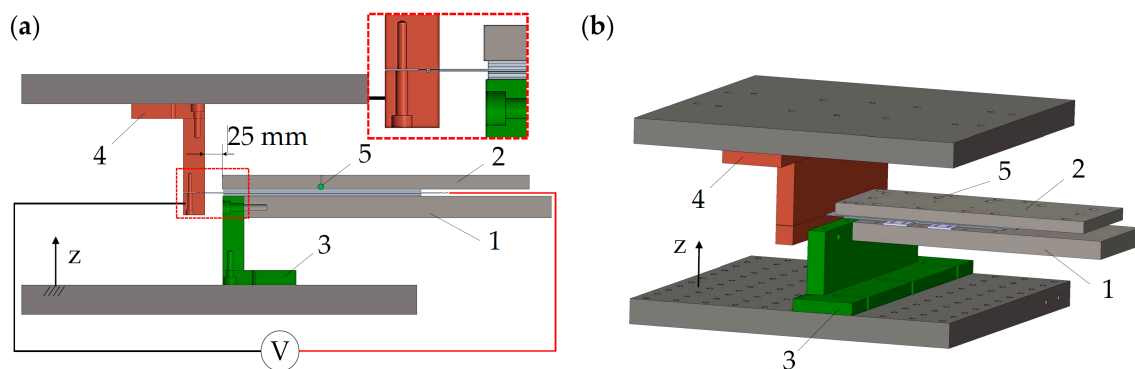
Figure 4. Test setup for the performed quasi-static mechanical tests. (1) Bottom plate. (2) Top plate. (3) Vertical connector. (4) Tab-clamping plate. (5) Thermocouple. (**a**) Cross-section and (**b**) 3D view.

After the clamping of the pouch cell electrode tabs, the bottom plate of the hydraulic press moved upwards (positive z-direction) with a speed of 0.1 mm/s to shear off the electrode tabs. The speed of 0.1 mm/s was chosen to achieve quasi-static conditions. The reaction force was measured with a load cell (GTM-K 25 kN, GTM Testing and Metrology GmbH, Bickenbach, Germany) of the accuracy class 0.02. A high-precision linear glass-scale

encoder (SINO KA-300, SINO, Sichuan, CHINA) with an accuracy of 1 μm was used to measure the displacement. A thermocouple Type K with ±0.75 °C was placed in the center of the pouch cell at the top plate (2) to monitor the temperature during the quasi-static mechanical test. The non-clamped electrode tab was wired with a bolt and a cable lug. The clamped electrode tab was electrically connected via wiring the tab-clamping plate (4).

Three tests were performed for each electrode tab (anode or cathode) of the pouch cell in order to investigate the differences in mechanical behavior and failure mode. The zero point of the displacement was set in the position where the clamped electrode tab was aligned with the tab-clamping plate (4) (no bending).

The point of short circuit was defined with a voltage drop of 0.05 V according to the literature [33].

3. Results

3.1. Component Tensile Tests

Figure 5 illustrates the statistical evaluation of the component tensile tests on the anode and cathode electrodes for MD and TD. The interquartile ranges and minimum and maximum values are indicated accordingly. The curves of the single experiments can be taken from Figure A1 in Appendix A.
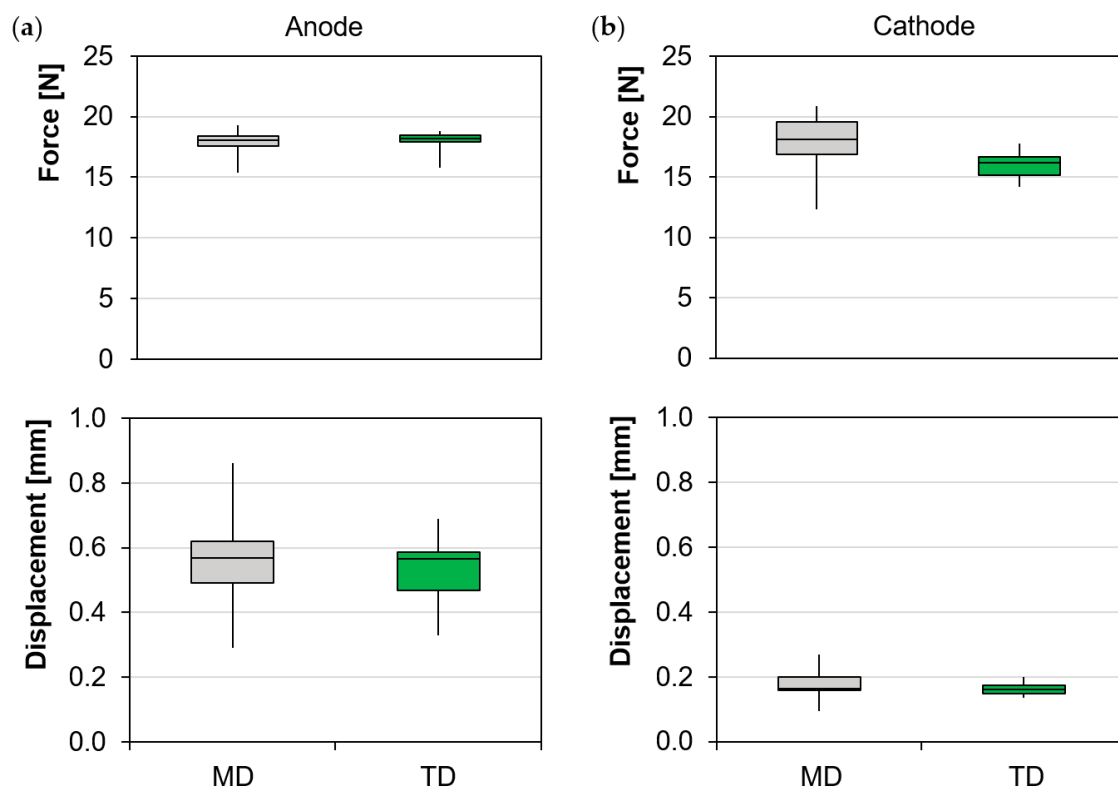
Figure 5. Statistical evaluation for force and displacement at fracture for MD (grey) and TD (green) directions of the tensile specimen. (**a**) Anode. (**b**) Cathode.

The anode did not indicate any anisotropy considering the force and displacement at fracture as the results of the MD and TD are similar. The force at fracture was, on average, 18.1 N (25.1 MPa) and 18.2 N (25.3 MPa) for MD and TD. The mean displacement at fracture was 0.57 mm and 0.56 mm for MD and TD.

In the case of the cathode, a difference in the force at fracture was observed for MD and TD, which is in line with the literature [34]. Zhang et al. [35] reported a difference in force at fracture between the MD and TD directions for low calendering pressure during electrode production, and attributed this behavior to the rolling in several passes during the production of the aluminum electrode carrier foil. The force at fracture was, on average,

18.1 N (18.9 MPa) and 16.2 N (16.9 MPa) for MD and TD. The displacement at fracture was on average 0.17 mm and 0.16 mm for MD and TD.

The cathode failed significantly earlier than the anode and, on average, was able to deform 70% less when compared to the anode. The force before fracture was, on average, the same for MD and was, in the case of TD, on average 11% smaller for the cathode when compared to the anode. Considering the tensile stress at fracture, the cathode revealed on average 25% and 33% smaller values for MD and TD when compared to the anode. Zhang et al. [35] found in a study that the graphite used for anodes indicates an increased adhesive strength after calendering and a tighter bond between the copper electrode carrier foil and the active material. On NMC cathodes, Zhang et al. found loose particles resulting from weak adhesion of the active material and aluminum current carrier foil which, overall, can explain the reduced fracture force when comparing the tensile test results of the anode and cathode within this study. The anode indicated a larger scatter for the displacement at fracture, as already observed in the literature [36].

Figure 6 illustrates the statistical evaluation of the tensile tests with the pouch foil. The maximum force at fracture was, on average, 44.1 N (49 MPa). The displacement at maximum force was, on average, 3.9 mm. The spread in the displacement at maximum force was large when compared to the anode or cathode. The cutting edge of the pouch foil specimen for tensile testing might indicate initial cracks. Zeng et al. [37] showed that the polypropylene layer of a pouch foil can restrain a further increase of cracks during tensile testing. Microscopic damages to the polypropylene layer of the pouch foil during specimen production will affect the crack propagation and can cause the observed scatter in failure displacement of the tensile tests with the pouch foil.
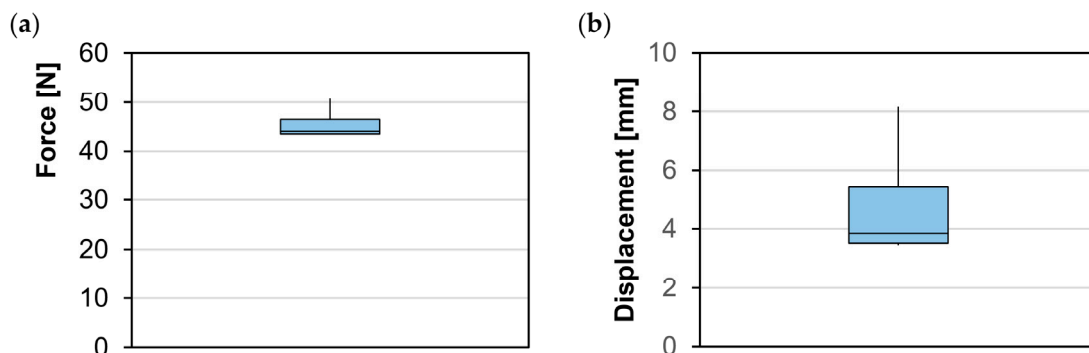
Figure 6. Statistical evaluation of the tensile tests with the pouch foil. (**a**) Maximum force. (**b**) Displacement at maximum force.

The polymer content of the pouch foil allows for a large deformation before a fracture occurs. Figure A2 in Appendix A illustrates the force–displacement curves of the single specimen. The polymer content of the pouch foil caused a constant mechanical resistance after the fracture of the aluminum inside the pouch foil, and is most likely caused by the polypropylene content of the pouch foil that can sustain an elongation of more than 600% [37].

The differences in the mechanical behavior of the anode and cathode are expected to affect the behavior of the pouch cell during quasi-static mechanical tests, depending on the tested electrode tab. The pouch foil is present on both sides and will not contribute to a possible difference between the electrode tabs. After the rupture of all tabs, a constant mechanical resistance can be expected, caused by the pouch foil.

3.2. Quasi-Static Mechanical Tests—Mechanical Behavior

Figure 7 illustrates the force–displacement and voltage–displacement curves of the quasi-static mechanical tests. Both the negative electrode tab (anode) and the positive electrode tab (cathode) indicated a similar mechanical behavior. The force increased sharply in the beginning and indicated a flat gradient until around 5 mm or 7 mm of displacement

for the negative and positive electrode tabs, respectively. After the flat gradient, the stiffness increased, indicated by the steep increase in force. The force drops abruptly after reaching a first force peak F_{max}^1 at a displacement d_{Fmax}^1. The first force peak F_{max}^1 ranged from 705.7 N to 858.8 N (avg. 782.9 N) for the negative electrode tab (anode) and from 619.1 N to 775.9 N (avg. 702.2 N) for the positive electrode tab (cathode). The first force peak F_{max}^1 occurred at displacement d_{Fmax}^1 between 9.5 mm and 9.6 mm (avg. 9.6 mm) for the negative electrode tab (anode) and between 10.5 mm and 12.8 mm (avg. 11.4 mm) for the positive electrode tab (cathode).
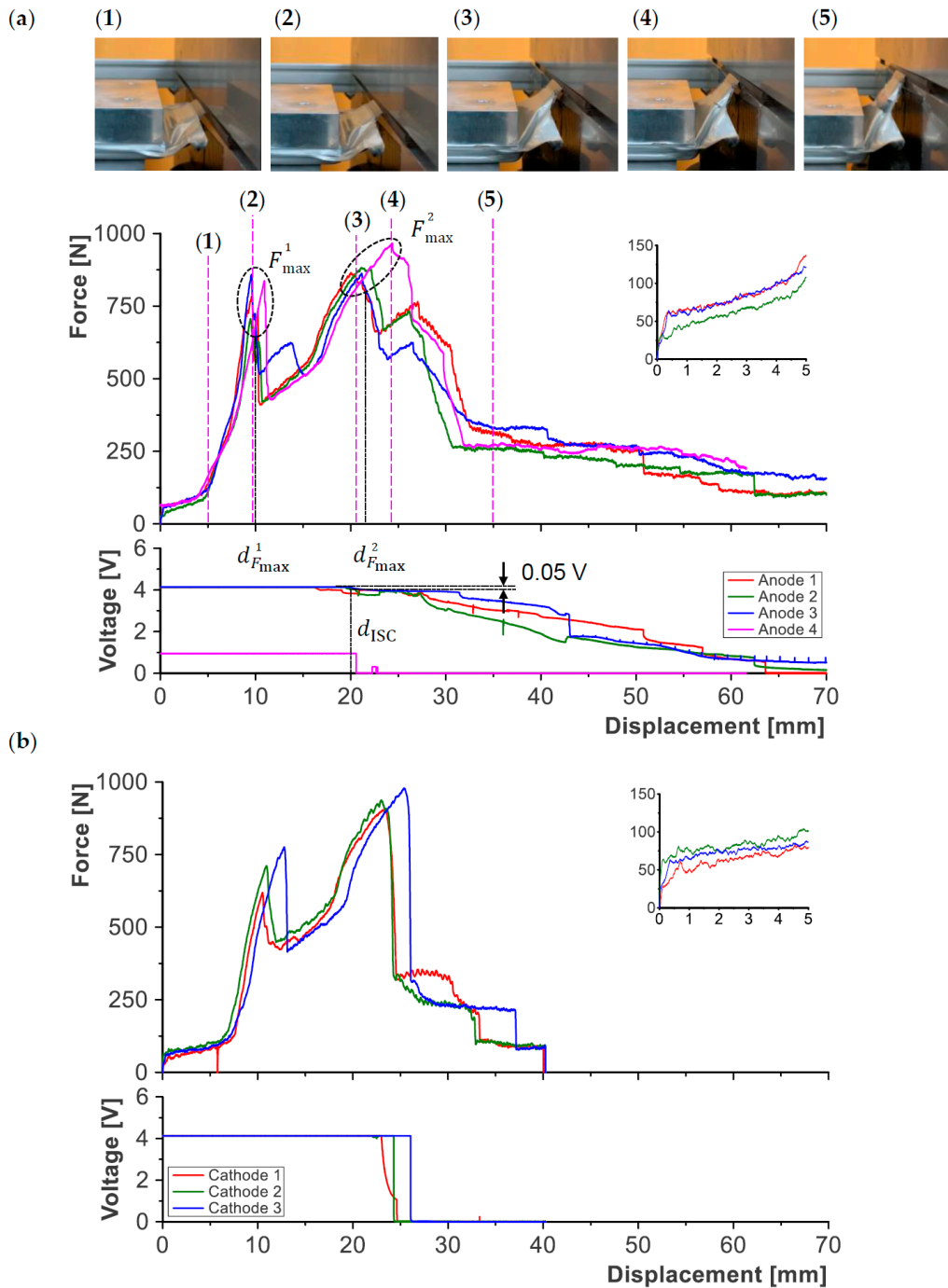
Figure 7. Force–displacement and voltage–displacement curves for the quasi-static mechanical tests with relevant force peaks F_{max}^1 and F_{max}^2 indicated by dotted circles. (**a**) Negative electrode tab (anode) with deformation pattern at displacement of (**1**) 5 mm, (**2**) 9 mm, (**3**) 21 mm, (**4**) 24 mm and (**5**) 35 mm for additional test at 0% SOC (Anode 4). (**b**) Positive electrode tab (cathode).

One test with the negative electrode tab (Anode 3) indicated an additional force drop before reaching the second force peak F^2_{max} at displacement $d^2_{F_{max}}$. This force peak can be attributed partly to a failure of the electrode tab. The second force peak F^2_{max} ranged from 862.9 N to 879.0 N (avg. 868.9 N) for the negative electrode tab (anode) and from 904.3 N to 978.9 N (avg. 940.3 N) for the positive electrode tab (cathode). The second force peak F^2_{max} occurred at displacement $d^2_{F_{max}}$ between 20.0 mm and 21.9 mm (avg. 21.0 mm) for the negative electrode tab (anode) and between 23.0 mm and 25.4 mm (avg. 23.9 mm) for the positive electrode tab (cathode). Table 2 summarizes the results of the single tests and the average values.

Table 2. Results and averages of first force peak F^1_{max} at displacement $d^1_{F_{max}}$, second force peak F^2_{max} at displacement $d^2_{F_{max}}$ and displacement at short circuit d_{ISC}.

Electrode	Test	F^1_{max} [N]		F^2_{max} [N]		$d^1_{F_{max}}$ [mm]		$d^2_{F_{max}}$ [mm]		d_{ISC} [mm]	
Negative (Anode)	1	784.2		864.8		9.6		20.0		16.5	
	2	705.7	782.9	879.0	868.9	9.5	9.6	21.9	21.0	19.6	18.8
	3	858.8		862.9		9.6		21.1		20.2	
Positive (Cathode)	1	619.1		904.3		10.5		23.2		23.0	
	2	711.5	702.2	937.8	940.3	10.9	11.4	23.0	23.9	24.2	24.4
	3	775.9		978.9		12.8		25.4		26.1	

The decrease in force after the first force peak F^1_{max} indicates that the internal structure of the pouch cell was partly failing. The mechanical failure of the structure resulted in a stiffness decrease after the first force peak F^1_{max}, indicated by the reduced slope of the force–displacement curve.

After the second force peak, a constant mechanical resistance was observed, with nearly no dependency on the electrode tab side. An analysis of the video data and a postmortem investigation revealed that this mechanical resistance could be attributed to the pouch foil. The second force peak F^2_{max} therefore clearly indicated a failure of the internal structure and will be discussed in more detail in the following section.

One additional test was performed on the negative electrode tab (Anode 4) with 0% SOC in order to confirm the aforementioned failure mechanism; see Figure 7. Using 0% SOC allowed for the use of a different test setup with better accessibility for recording, and did not seem to have a significant impact on the force–displacement curve when compared to the experiments performed at 100% SOC.

The pouch foil continuously straightens as the displacement increases and initiates a tension in the current conductor foils (Figure 7(1)) until the failure of the internal structures indicated by the first force peak F^1_{max} (Figure 7(2)). A rearrangement of the internal structure can be observed from a displacement of 21 mm (Figure 7(3)).

The displacement of 24 mm (Figure 7(4)) corresponded to the second force peak F^2_{max}. The subsequent drop in force can be associated with the formation of cracks within the pouch foil, in particular in the aluminum portion of the pouch foil. The force gradually decreases as the cracks propagate through the aluminum portion of the pouch foil, and stabilizes only when the polymer portion of the pouch foil is left over as mechanical resistance (Figure 7(5)).

However, the voltage displacement behavior seemed to be affected by the other test setup. A difference in kinematics during sequential deformation caused an instantaneous drop in voltage after the mechanical failure of the current conductor flags. For the experiment with Anode 4, the position of the pouch cell was fixed and the electrode tab was moving upwards whereas, for the other experiments, the electrode tab was in a fixed position and the pouch cell was moving upwards.

3.3. Quasi-Static Mechanical Tests—Failure Behavior

The voltage–displacement curve in Figure 7 illustrates a significant difference between the negative electrode tab (anode) and positive electrode tab (cathode). The voltage, in the case of testing with the negative electrode tab (anode), indicated a step-wise drop in voltage with increasing displacement. The voltage started to decrease before the second force peak F_{max}^2, indicating the failure of the internal structure. The voltage drop d_{ISC} ranged from 16.5 mm to 20.2 mm (avg. 18.8 mm); see Table 2. The displacement at short circuit d_{ISC} occurred, on average, 2.2 mm earlier than the second force peak. A possible explanation for this short circuit behavior is the sequential rupture of single current conductor flags inside the pouch cell. A postmortem analysis confirmed that the current conductor flags ruptured sequentially after each other in front of the welding points. Figure 8a illustrates postmortem photos after the quasi-static mechanical test with the negative electrode tab (anode). The torn-out tab has some remaining parts of the copper current conductor flags attached to the welded area. All current conductor flags ruptured inside the pouch foil in the area of the welded area. The polymer content of the pouch foil was still intact but severely deformed. The aluminum of the pouch foil was ruptured. The polymer content of the pouch foil caused the constant mechanical resistance observed after the second force peak. Apart from that, the pouch foil indicated a strong deformation and a formation of two folds. Anode 3 indicated an additional rupture on the electrode tab causing the additional force peak indicated in Figure 7.
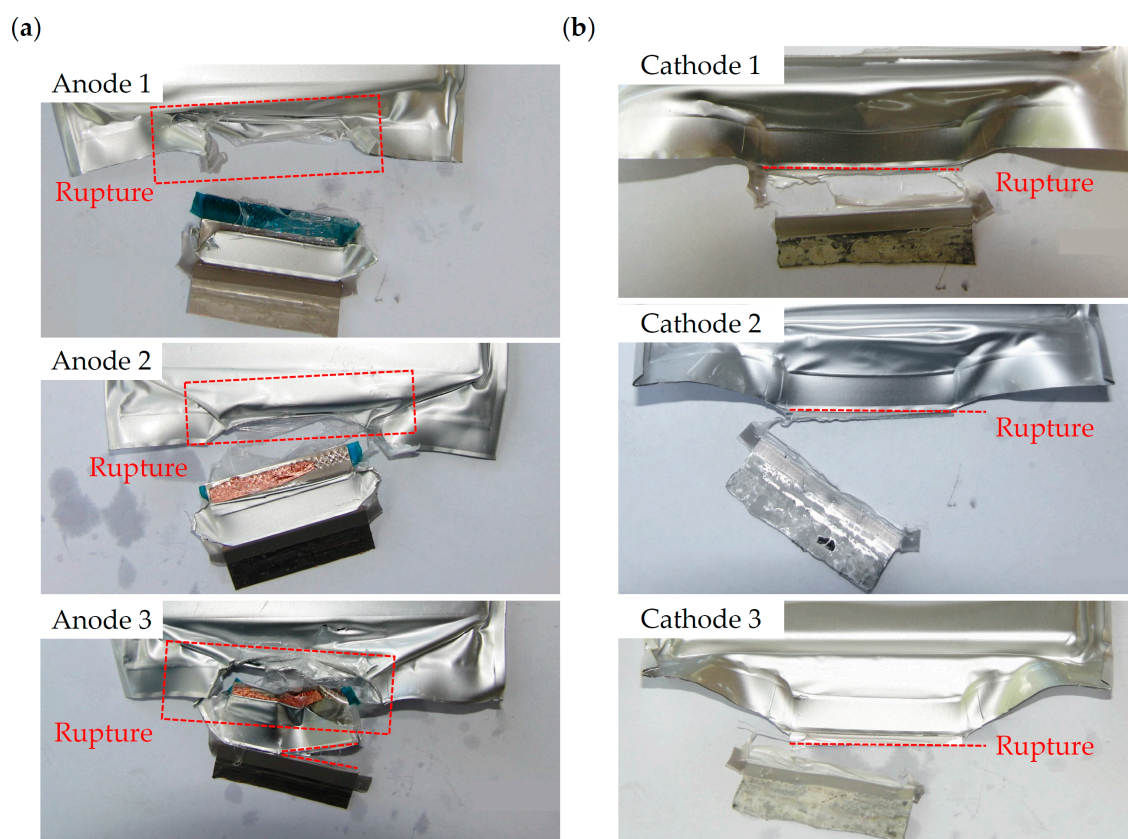
Figure 8. Postmortem photos after the quasi-static mechanical test. (**a**) Negative electrode tab (anode). (**b**) Positive electrode tab (cathode).

The voltage dropped abruptly in the case of the positive electrode tab (cathode) and almost coincided with the second force peak. The voltage drop d_{ISC} occurred slightly later than the second force peak ranging from 23.0 mm to 26.1 mm (avg. 24.4 mm), and was on average 0.5 mm later than the second force peak; see Table 2. This was attributed to another failure mechanism compared to the negative electrode tab (anode) and was validated with

a postmortem analysis. The tab ruptured on the outside of the pouch foil without damaging the pouch foil. Figure 8b illustrates a postmortem photo after the quasi-static mechanical test with the positive electrode tab (cathode). The positive electrode tab ruptured close to the clamping point at the area of the tab sealing. The electrode tab sealing is welded with the pouch foil during the manufacturing process and caused the constant mechanical resistance after the second force peak.

The quasi-static mechanical test can be simplified using a kinematic problem. A movement of the tab results in an elongation of the current conductor flags, causing a tensile load. Further displacement of the electrode tab increases the tensile load of the current conductor flag until the load limit of single foils is reached and rupture occurs.

The thickness of the aluminum carrier foil on the positive electrode tab (cathode) is twice in thickness when compared to the copper carrier foil on the negative electrode tab (anode) side. It can be assumed that the larger thickness results in the higher mechanical resistance of the positive electrode tab (cathode), even though the tensile tests show an earlier failure of the cathode electrodes. The aluminum current conductor flags were able to carry a higher mechanical load, resulting in a rupture outside of the pouch foil. In the case of the copper current conductor flags, the flags were failing sequentially one after the other when reaching the mechanical load limit.

No thermal runaway was triggered by the mechanical deformation and the failure mode observed during the quasi-static mechanical tests. No change in the temperature was observed. In the case of the negative electrode tab (anode), some electrolyte leaked from the ruptured pouch foil.

4. Conclusions

In this study, six quasi-static mechanical tests were performed with commercial pouch cells at 100% SOC by shearing off the negative (anode) or positive (cathode) electrode tab. Tensile tests were conducted on the anode, cathode and pouch foil of the pouch cell to explain differences in the quasi-static mechanical tests for the negative (anode) and positive (cathode) electrode tabs.

The quasi-static mechanical tests for the negative (anode) and positive (cathode) electrode tabs indicated two force peaks before failure. The negative electrode tab (anode) failed inside the pouch foil through a rupture of the single electrode carrier foils. The positive electrode tab (cathode) failed through a rupture of the whole electrode tab outside of the pouch foil. The negative electrode tab (anode) was able to withstand on average a 7.6% smaller maximum force and 23.0% smaller displacement at voltage drop when compared to the positive electrode tab (cathode). The differences in the failure behavior are attributed to the mechanical properties of the single electrode carrier foils. The current conductor flags have the same length as the electrode tab, and the shearing movement causes tension at the current conductor flags, which is greatest at the current conductor flag that is furthest away from the relative movement of the electrode tab. The main conclusions of this study are summarized as follows:

- The negative electrode tab (anode) is more dangerous in case of an electrode tab shear-off as the pouch cell opens and the current conductor flags rupture. This leads to a leakage of electrolyte and, in the worst case, the exposed current conductor flags can trigger an internal short circuit. No thermal runaway occurred during or directly after the quasi-static mechanical tests for both the negative electrode tab (anode) and positive electrode tab (cathode). However, the opened pouch foil, in the case of the negative electrode tab (anode), triggers exothermal chemical reactions with the ambient atmosphere, potentially causing severe consequences.

The described issues and failure mechanisms have to be investigated in more detail in order to avoid critical situations when deformations occur in the area of the electrode tabs. This is not only limited to Lithium-ion pouch cells but also to other types of battery systems (e.g., sodium-ion pouch cells), as the failure mode is a purely mechanical issue. An optimization of the negative electrode tab (anode) should be considered to increase the

safety of pouch cells. An adaptive length for the current conductor flags, optimized for the kinematic problem that occurs during a deformation of the electrode tab, could address the aforementioned issues. Another approach to making the electrode tab area safer could be the inclusion of a predetermined breaking point for the electrode tab to avoid an opening of the pouch foil. Additionally, in future research, the mechanical and failure behavior should be investigated after electrochemical cycling to investigate potential material degradation.

Author Contributions: Conceptualization, P.H. and S.F.H.; methodology, P.H. and S.F.H.; validation, P.H.; formal analysis, P.H.; investigation, P.H.; data curation, P.H.; writing—original draft preparation, P.H.; writing—review and editing, P.H., S.F.H. and C.E.; visualization, P.H.; supervision, C.E.; project administration, S.F.H.; funding acquisition, S.F.H. All authors have read and agreed to the published version of the manuscript.

Data Availability Statement: The data presented in this study are available on request from the corresponding author. The data are not publicly available due to privacy restrictions.

Conflicts of Interest: The authors declare no conflicts of interest.

Abbreviations

The following abbreviations are used in this manuscript:

LIB	Lithium-ion battery
Ni	Nickel
NMC	Nickel Manganese Cobalt
MD	Machine direction
SOC	State of charge
TD	Transverse direction

Appendix A

Figure A1 illustrates the results of the tensile tests performed on the anode and cathode for MD and TD.
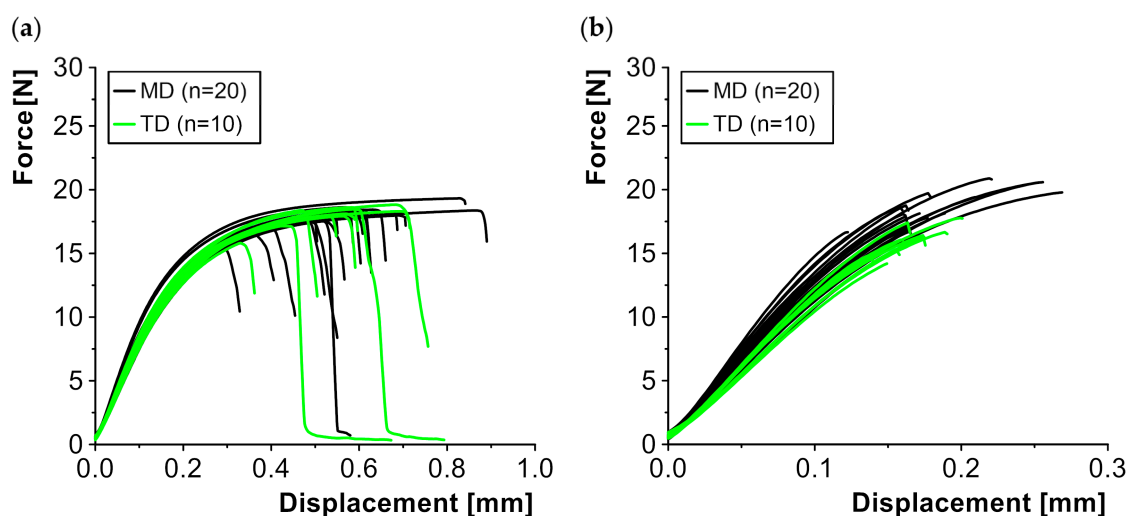
Figure A1. Force–displacement curves of the component tensile tests with MD and TD orientation. (**a**) Anode. (**b**) Cathode.

Figure A2 illustrates the results of the tensile tests performed on the pouch foil.
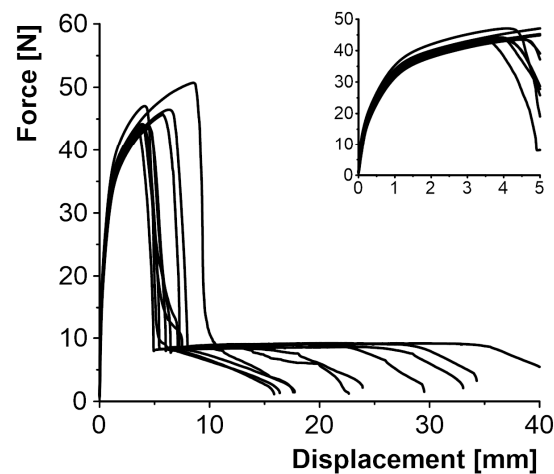

Figure A2. Force–displacement curves of the component tensile tests with the pouch foil.

References

1. Zeng, X.; Li, M.; Abd El-Hady, D.; Alshitari, W.; Al-Bogami, A.S.; Lu, J.; Amine, K. Commercialization of Lithium Battery Technologies for Electric Vehicles. *Adv. Energy Mater.* **2019**, *9*, 1900161. [CrossRef]
2. Feng, X.; Ouyang, M.; Liu, X.; Lu, L.; Xia, Y.; He, X. Thermal runaway mechanism of lithium ion battery for electric vehicles: A review. *Energy Storage Mater.* **2018**, *10*, 246–267. [CrossRef]
3. Camargos, P.H.; dos Santos, P.H.J.; dos Santos, I.R.; Ribeiro, G.S.; Caetano, R.E. Perspectives on Li-ion battery categories for electric vehicle applications: A review of state of the art. *Int. J. Energy Res.* **2022**, *46*, 19258–19268. [CrossRef]
4. Arief Budiman, B.; Rahardian, S.; Saputro, A.; Hidayat, A.; Pulung Nurprasetio, I.; Sambegoro, P. Structural integrity of lithium-ion pouch battery subjected to three-point bending. *Eng. Fail. Anal.* **2022**, *138*, 106307. [CrossRef]
5. Fasching, M.; Grollitsch, S.; Höschele, P.; Schmid, A.; Ellersdorfer, C. Investigating the mechanical in-plane characteristics of lithium-ion pouch cells under crush loads. *J. Energy Storage* **2024**, *89*, 111581. [CrossRef]
6. Höschele, P.; Heindl, S.F.; Erker, S.; Ellersdorfer, C. Influence of reversible swelling and preload force on the failure behavior of a lithium-ion pouch cell tested under realistic boundary conditions. *J. Energy Storage* **2023**, *65*, 107228. [CrossRef]
7. Samba, A.; Omar, N.; Gualous, H.; Capron, O.; van den Bossche, P.; van Mierlo, J. Impact of Tab Location on Large Format Lithium-Ion Pouch Cell Based on Fully Coupled Tree-Dimensional Electrochemical-Thermal Modeling. *Electrochim. Acta* **2014**, *147*, 319–329. [CrossRef]
8. Lee, D.-C.; Lee, J.-J.; Kim, J.-S.; Cho, S.; Kim, C.-W. Thermal behaviors analysis of 55 Ah large-format lithium-ion pouch cells with different cell aspect ratios, tab locations, and C-rates. *Appl. Therm. Eng.* **2020**, *175*, 115422. [CrossRef]
9. Baek, I.; Kang, D.; Batool, D.; Choi, C.; Kwak, B.; Na, W.; Kim, J. An experimental investigating on the effect of contact resistance for pouch-type lithium-ion batteries on the performance and safety. In Proceedings of the 2022 IEEE Energy Conversion Congress and Exposition (ECCE), Detroit, MI, USA, 9–13 October 2022; pp. 1–5. [CrossRef]
10. Mei, W.; Chen, H.; Sun, J.; Wang, Q. Numerical study on tab dimension optimization of lithium-ion battery from the thermal safety perspective. *Appl. Therm. Eng.* **2018**, *142*, 148–165. [CrossRef]
11. Chang, H.; Lee, J.; Kim, C.-W. A statistical analysis of thermal characteristics of 55-Ah large-format LIB pouch cell with different tab-type, tab size, and tab position. *Case Stud. Therm. Eng.* **2022**, *30*, 101777. [CrossRef]
12. Das, A.; Barai, A.; Masters, I.; Williams, D. Comparison of Tab-To-Busbar Ultrasonic Joints for Electric Vehicle Li-Ion Battery Applications. *World Electr. Veh. J.* **2019**, *10*, 55. [CrossRef]
13. Günter, F.J.; Wassiliadis, N. State of the Art of Lithium-Ion Pouch Cells in Automotive Applications: Cell Teardown and Characterization. *J. Electrochem. Soc.* **2022**, *169*, 30515. [CrossRef]
14. Shin, H.-S.; de Leon, M. Mechanical performance and electrical resistance of ultrasonic welded multiple Cu-Al layers. *J. Mater. Process. Technol.* **2017**, *241*, 141–153. [CrossRef]
15. Balz, I.; Rosenthal, E.; Reimer, A.; Turiaux, M.; Schiebahn, A.; Reisgen, U. Analysis of the thermo-mechanical mechanism during ultrasonic welding of battery tabs using high-speed image capturing. *Weld. World* **2019**, *63*, 1573–1582. [CrossRef]
16. Grabmann, S.; Kriegler, J.; Harst, F.; Günter, F.J.; Zaeh, M.F. Laser welding of current collector foil stacks in battery production–mechanical properties of joints welded with a green high-power disk laser. *Int. J. Adv. Manuf. Technol.* **2022**, *118*, 2571–2586. [CrossRef]
17. Zwicker, M.F.R.; Moghadam, M.; Zhang, W.; Nielsen, C.V. Automotive battery pack manufacturing—A review of battery to tab joining. *J. Adv. Join. Processes* **2020**, *1*, 100017. [CrossRef]

18. Brand, M.J.; Schmidt, P.A.; Zaeh, M.F.; Jossen, A. Welding techniques for battery cells and resulting electrical contact resistances. *J. Energy Storage* **2015**, *1*, 7–14. [CrossRef]

19. Brand, M.J.; Kolp, E.I.; Berg, P.; Bach, T.; Schmidt, P.; Jossen, A. Electrical resistances of soldered battery cell connections. *J. Energy Storage* **2017**, *12*, 45–54. [CrossRef]

20. Mypati, O.; Mishra, D.; Sahu, S.; Pal, S.K.; Srirangam, P. A Study on Electrical and Electrochemical Characteristics of Friction Stir Welded Lithium-Ion Battery Tabs for Electric Vehicles. *J. Electron. Mater.* **2020**, *49*, 72–87. [CrossRef]

21. Liu, Y.; Zhang, R.; Wang, J.; Wang, Y. Current and future lithium-ion battery manufacturing. *iScience* **2021**, *24*, 102332. [CrossRef] [PubMed]

22. Das, A.; Li, D.; Williams, D.; Greenwood, D. Joining Technologies for Automotive Battery Systems Manufacturing. *World Electr. Veh. J.* **2018**, *9*, 22. [CrossRef]

23. Kukreja, J.; Nguyen, T.; Siegmund, T.; Chen, W.; Tsutsui, W.; Balakrishnan, K.; Liao, H.; Parab, N. Crash analysis of a conceptual electric vehicle with a damage tolerant battery pack. *Extrem. Mech. Lett.* **2016**, *9*, 371–378. [CrossRef]

24. Scurtu, L.; Szabo, I.; Mariasiu, F.; Moldovanu, D.; Mihali, L.; Jurco, A. Numerical analysis of the influence of mechanical stress on the battery pack's housing of an electric vehicle. *IOP Conf. Ser. Mater. Sci. Eng.* **2019**, *568*, 12054. [CrossRef]

25. Li, R.; Li, W.; Singh, A.; Ren, D.; Hou, Z.; Ouyang, M. Effect of external pressure and internal stress on battery performance and lifespan. *Energy Storage Mater.* **2022**, *52*, 395–429. [CrossRef]

26. Michelini, E.; Höschele, P.; Heindl, S.F.; Erker, S.; Ellersdorfer, C. Experimental Investigation on Reversible Swelling Mechanisms of Lithium-Ion Batteries under a Varying Preload Force. *Batteries* **2023**, *9*, 218. [CrossRef]

27. Zeng, Z.; An, X.; Peng, C.; Ruan, X.; Song, Z.; Dang, C.; An, Z. Study on the thermal runaway behavior and mechanism of 18650 lithium-ion battery induced by external short circuit. *Appl. Therm. Eng.* **2025**, *258*, 124569. [CrossRef]

28. Dong, T.; Wang, Y.; Peng, P.; Jiang, F. Electrical-thermal behaviors of a cylindrical graphite- NCA Li -ion battery responding to external short circuit operation. *Int. J. Energy Res.* **2019**, *43*, 1444–1459. [CrossRef]

29. Duan, J.; Tang, X.; Dai, H.; Yang, Y.; Wu, W.; Wei, X.; Huang, Y. Building Safe Lithium-Ion Batteries for Electric Vehicles: A Review. *Electrochem. Energy Rev.* **2020**, *3*, 1–42. [CrossRef]

30. Ruiz, V.; Pfrang, A.; Kriston, A.; Omar, N.; van den Bossche, P.; Boon-Brett, L. A review of international abuse testing standards and regulations for lithium ion batteries in electric and hybrid electric vehicles. *Renew. Sustain. Energy Rev.* **2018**, *81*, 1427–1452. [CrossRef]

31. Zhu, J.; Wierzbicki, T.; Li, W. A review of safety-focused mechanical modeling of commercial lithium-ion batteries. *J. Power Sources* **2018**, *378*, 153–168. [CrossRef]

32. Balz, I.; Raad, E.A.; Rosenthal, E.; Lohoff, R.; Schiebahn, A.; Reisgen, U.; Vorländer, M. Process monitoring of ultrasonic metal welding of battery tabs using external sensor data. *J. Adv. Join. Processes* **2020**, *1*, 100005. [CrossRef]

33. Liu, B.; Jia, Y.; Yuan, C.; Wang, L.; Gao, X.; Yin, S.; Xu, J. Safety issues and mechanisms of lithium-ion battery cell upon mechanical abusive loading: A review. *Energy Storage Mater.* **2020**, *24*, 85–112. [CrossRef]

34. Wang, L.; Yin, S.; Zhang, C.; Huan, Y.; Xu, J. Mechanical characterization and modeling for anodes and cathodes in lithium-ion batteries. *J. Power Sources* **2018**, *392*, 265–273. [CrossRef]

35. Zhang, J.; Sun, J.; Huang, H.; Ji, C.; Yan, M.; Yuan, Z. Deformation and fracture mechanisms in the calendering process of lithium-ion battery electrodes. *Appl. Energy* **2024**, *373*, 123900. [CrossRef]

36. Liu, Y.; Xia, Y.; Zhou, Q. Effect of low-temperature aging on the safety performance of lithium-ion pouch cells under mechanical abuse condition: A comprehensive experimental investigation. *Energy Storage Mater.* **2021**, *40*, 268–281. [CrossRef]

37. Zeng, F.; Chen, J.; Yang, F.; Kang, J.; Cao, Y.; Xiang, M. Effects of Polypropylene Orientation on Mechanical and Heat Seal Properties of Polymer-Aluminum-Polymer Composite Films for Pouch Lithium-Ion Batteries. *Materials* **2018**, *11*, 144. [CrossRef] [PubMed]